J Appl Electrochem (2011) 41:741–749
DOI 10.1007/s10800-011-0290-3

ORIGINAL PAPER

Effect of sodium chloride on corrosion of mild steel in CO_2-saturated brines

Jiabin Han · J. William Carey · Jinsuo Zhang

Received: 18 January 2011 / Accepted: 13 March 2011 / Published online: 30 March 2011

Abstract Corrosion rates of mild steel were measured in oxygen-free, CO_2-saturated brines as a function of NaCl concentration employing electrochemical techniques. Decreased corrosion rates were observed as salt concentration increased. However, at high salt concentration ($\geq$20 wt% NaCl), corrosion rates were independent of the flow rate of CO_2-saturated brine. To understand this phenomenon, corrosion surfaces were analyzed by scanning electron microscopy and X-ray diffraction and showed only residual iron carbide for salt concentrations of 0.5–5 wt%. However, at 20 wt% NaCl, a porous corrosion scale with embedded crystals, possibly magnetite, was observed. No iron carbonate was observed and water chemistry showed it was 10,000 times below saturation. A numerical model of corrosion in CO_2–NaCl systems was able to predict the reduced corrosion rates with salt concentration increase as a consequence of reduced solubility of CO_2 ("salting-out"). However, the model did not predict that corrosion rates were flow-independent at high salt concentration. These results demonstrate that flow-independent corrosion is a consequence of a diffusion barrier created by magnetite scale, present only at high salt concentrations.

Keywords Carbon dioxide · Salt · Corrosion · Scale · Electrochemistry · Water chemistry · Geologic sequestration · Analytical method

J. Han (✉) · J. W. Carey
Earth and Environmental Sciences Division, Los Alamos National Laboratory, Los Alamos, NM 87545, USA
e-mail: jhan@lanl.gov; jiabin.han@gmail.com

J. Zhang
Decision and Application Division, Los Alamos National Laboratory, Los Alamos, NM 87545, USA

1 Introduction

Control of greenhouse gas emissions is increasingly recognized as a critical environmental concern [1]. One of the proposed methods to control carbon emissions to the atmosphere is the geologic sequestration of CO_2, which involves injecting high-pressure supercritical CO_2 via wells into natural reservoirs with the objective of permanent storage [2, 3]. Wellbore systems are constructed using steel and cement and are one of the principal risks of CO_2 leakage back to the atmosphere. Field studies by Carey et al. [4] and Crow et al. [5] identified critical CO_2 leakage paths in wellbore systems to be interfaces between steel casing and cement and between cement and rock. If escaping CO_2 infiltrates the cement–steel interface, corrosion can be severe because saline water within the interface will be saturated with high-pressure CO_2 [6, 7]. Typical geologic sequestration environments are high temperature (40–120 °C), high-pressure (100–500 bars), and high-salinity (10,000–200,000 ppm) environments. Most of the available corrosion models are not able to represent these extreme conditions [8, 9]. In particular, we found that water chemistry was not well represented due to the high-salinity environment, which limits model application. We recently have developed a mechanistic electrochemical corrosion model coupling an accurate water chemistry model applied for these extreme geologic conditions [10]. The model correctly predicts reduced corrosion rates as salinity increases in CO_2-saturated brined due to reduced solubility of CO_2 or in other words, the "salting-out" effect of sodium chloride.

Chloride is well known to play a crucial role in steel corrosion, but its effect depends on whether the aqueous system is deaerated (oxygen-free), oxygen-aerated, or deaerated but CO_2-bearing. In deaerated acidic solutions,

chloride accelerates the anodic kinetics of iron dissolution via a catalytic mechanism [11–14]. In deaerated neutral and alkaline solutions, a corrosion scale is usually formed. Asakura and Nobe [15] found chloride accelerates steel anodic corrosion kinetics in this environment through formation of additional chloride reaction paths. Burstein et al. [16–18] developed a surface scratch technique to investigate monolayer corrosion film under these conditions and found that chloride accelerates the reaction rate of a freshly generated surface. This was explained by corrosion occurring via a chloride pathway in which chloride forms intermediate corrosion species and accelerates corrosion kinetics by a factor of 100 [18]. In most of these studies, scale formation was not considered. However, Wang et al. [19] used surface analysis methods and observed iron oxide scale formation in deaerated high-ionic strength brines at room temperature. We hypothesize that scale formation may also play a key role in determining corrosion rates in high-ionic strength systems containing CO_2.

In oxygen or air-saturated systems, the oxygen-induced corrosion mechanism involves oxygen mass transfer (slow step), followed by electrochemical reaction (fast) on the steel surface [20]. A minor increase in corrosion rate is observed at low chloride concentration up to 3 wt%, and then corrosion rates are decreased by increasing chloride concentration [21, 22]. The corrosion rate decrease was attributed to salting-out of dissolved oxygen at higher chloride concentrations [20–22]. We consider "salting-out" as another crucial role of salt in CO_2-bearing systems.

Fang et al. [23, 24] investigated the effect of sodium chloride in deaerated, CO_2-bearing brines on corrosion of typical pipeline material (mild steel C1018) at pH 4–6, temperature 0−20 °C, NaCl concentration 3−25 wt% saturated with CO_2 at 1 bar fixed partial pressure. Using potentiodynamic sweep measurements, both anodic and cathodic current densities were shown to decrease with increasing salt concentration. The limiting current density, which is determined by mass transfer, was also reduced by salt. Thus, in the absence of oxygen, corrosion rates of mild steel were reduced at higher salt (NaCl) concentration. In contrast to typical corrosion behavior and model predictions, Fang et al. [23, 24] also observed that corrosion rates had little dependence on CO_2-brine flow rates at low temperature 0−5 °C and high NaCl concentration between 20 and 25 wt%.

In this study, we show that in deaerated, CO_2-bearing systems NaCl affects corrosion rates through changes in water chemistry that reduces dissolved CO_2, which reduces corrosion kinetics. In addition, we investigate the mechanism leading to flow-independent corrosion kinetics in highly concentrated brines, as observed by Fang et al. [23, 24]. Corrosion experiments were conducted at 25 °C in oxygen-free environments with CO_2 as a function of NaCl concentration. The corrosion surface was examined using scanning and backscattered electron microscopy (SEM and BSE), energy dispersive spectroscopy (EDX), and X-ray diffraction (XRD) to determine corrosion mechanisms. The experiments were used to test our corrosion model [10] at low CO_2 pressure and high-salinity conditions. The model was then used to understand potential mechanisms for the flow-independent corrosion behavior of high-salinity, O_2-free, CO_2-systems.

Our motivation for this study is the study of wellbore integrity in geologic CO_2 sequestration. In this environment, high-salinity brines are common and there is the potential for long-term exposure of steel to CO_2-bearing fluids. Our particular focus is the external environment of the wellbore systems where the native brines are generally oxygen-free. (We do not consider CO_2–O_2 systems here, but in some sequestration scenarios, minor amounts of oxygen may be co-injected with the CO_2). Steel is a critical component of the well barrier system, and our study seeks to develop a quantitative understanding of the service life of carbon steel in CO_2 sequestration reservoirs. Flow rate is a key variable in corrosion analyses, and flow of CO_2-bearing brines at the cement–steel or steel–rock annulus is likely to be very slow to stagnant depending on pressure gradients and the effective permeability of the wellbore exterior. Thus, flow-induced uniform corrosion on bare steel is at a minimum. We note that both the low flow rate of the brines and the high concentration of Cl^- are likely to significantly impact localized corrosion rates, however, this is not within the scope of the study.

2 Experimental methods

Corrosion tests were carried out employing a classical three-electrode electrochemical glass cell setup. The reference was a calomel electrode with saturated KCl-filling solution. The counter electrode was a titanium rod. The working electrode was J55 mild steel with composition given in Table 1. This steel is commonly used in wellbore completions.

Table 1 The J55 steel chemical composition (wt%)

Al	B	C	Ca	Cr	Cu
0.018	0.0001	0.36	0.0014	0.100	0.170
Mn	Mo	N	Nb	Ni	P
1.020	0.020	0.0099	0.001	0.070	0.007
S	Si	Sn	Ti	V	Fe
0.003	0.280	0.008	0.027	0.002	Balance

Corrosion of J55 mild steel was tested at a variety of different NaCl concentrations in ambient CO_2 saturated aqueous environments (Table 2). The corrosion rate was measured using linear polarization resistance (LPR) and electrochemical impedance spectroscopy (EIS) techniques. LPR measures the total circuit resistance including solution resistance and corrosion resistance. EIS measures the solution resistance at high frequency (e.g., 100 kHz) and total resistance at low frequency (e.g., 10 mHz). The corrosion resistance was obtained by LPR and EIS or by EIS alone (as the diameter of the semi-sphere Nyquist plot).

Prior to the experiments, the NaCl solution was deaerated with CO_2 for at least 1 h and the temperature was controlled at 25 °C. Solution pH was adjusted by sodium bicarbonate (1 mol L^{-1}) and then purged with CO_2 for another hour. The rectangular J55 coupon was soldered with a conductive cable and the junction was embedded in epoxy to isolate the soldered area. The steel coupon was embedded in epoxy and a 2 × 1 cm^2 surface was exposed by grinding. The exposed steel surface was sequentially polished with 220 and 600 grit carbide abrasive paper. Isopropanol was sprayed on the sample in order to cool it during the grinding and polishing procedure. The sample was rinsed in isopropanol, ultrasonically cleaned, and blown dry. The sample was immersed into the prepared electrolyte solution and its corrosion rate was measured employing a BioLogic SP-150 electrochemical instrument. The corrosion surfaces were analyzed in-house using an FEI® SEM with EDX and a Siemens® XRD on uncoated samples. The composition of corrosion solution samples was analyzed using Dionex® Ion Chromatography, inductively coupled plasma-optical emission spectroscopy (ICP-OES) methods, and by alkalinity titration.

Table 2 Test conditions for corrosion experiments

Electrode material	J55 mild steel
Electrode surface area (cm^2)	2
T (°C)	25
pH	4
pCO_2 (bar)	0.97
NaCl (wt%)	0.5, 1, 5, 20
Stirring speed (rpm)	100–800
Test period (day)	3–4
Electrochemical measurements	LPR, EIS
Analysis	SEM, EDX, XRD
LPR	
Polarization range vs. OCP (mV)	±10
Scan rate (mV s^{-1})	0.2
EIS	
Frequency range (Hz)	0.01–200000
Peak to peak amplitude (mV)	20

3 Experimental results

3.1 Corrosion rate measurements at different NaCl concentrations

The corrosion rate was determined by electrochemical measurements using the formula [25]:

$$CR = \frac{i_{\text{corr}} M_{\text{Fe}}}{\rho_{\text{Fe}} n F} = 1.155 i_{\text{corr}} = 1.155 \frac{B}{R_c} \quad (1)$$

where CR is corrosion rate (mm $year^{-1}$), i_{corr} is corrosion current density (A m^{-2}), M_{Fe} is the molecular weight of iron, ρ_{Fe} is the density of steel, n is the number of electrons exchanged in the electrochemical reaction, F is Faraday's constant, 1.155 is the material-dependent constant appropriate for carbon steel, R_c is the corrosion resistance (Ω) measured by combined LPR and EIS and the B value is a function of temperature and is defined by [26]:

$$B = \beta_a \times \beta_c / [2.303(\beta_a + \beta_c)] \quad (2)$$

where β_a is the anodic Tafel slope for iron dissolution [25, 26]:

$$\beta_a = 2.303 \frac{RT}{\alpha_a F} \quad (3)$$

β_c is the cathodic Tafel slope defined as [25]:

$$\beta_c = 2.303 \frac{RT}{\alpha_c F} \quad (4)$$

where R is the gas constant, T is temperature in K, and α is the transfer coefficient of iron dissolution reaction for unit reaction. According to Bockris, the apparent $\alpha_a = 1.5$ and $\alpha_c = 0.5$ for anodic and cathodic reactions on iron surfaces in acidic environments [27].

The experimental corrosion rate decreases as salt concentration increases from 0.5–20 wt% at stirring speeds from 100 to 800 rpm (Fig. 1). At NaCl concentration <20 wt%, the corrosion rates increase as stirring speed increases. Whereas, we observed that in highly

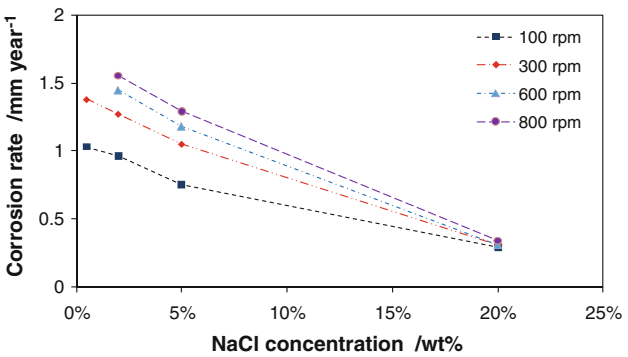

Fig. 1 Corrosion rate as a function of NaCl concentration at different stirring speed rates at pH = 4, T = 25 °C, and pCO_2 = 0.97 bar

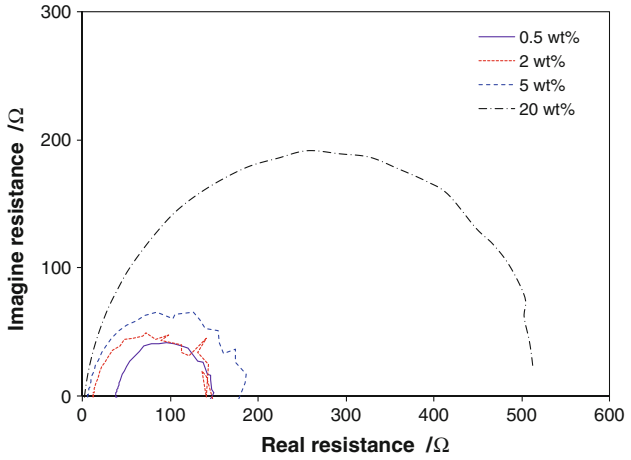

Fig. 2 Nyqist plot of EIS measurements as a function of NaCl concentration at pH = 4, $T = 25$ °C, stirring speed $\omega = 300$ rpm, and $pCO_2 = 0.97$ bar

concentrated solutions (20 wt% NaCl), corrosion rates are independent of brine flow rates, in agreement with previous observations for carbon steel C1018 made at 5 °C [23, 24].

EIS measurements (Fig. 2) show corrosion resistance (proportional to the diameter of the semicircle) increases and solution resistance decreases as salt concentration increases in agreement with calculations from combined LPR and EIS. The solution resistance at low salt concentration 0.5% is 50 Ω, which is large enough to be considered during LPR measurements. The semicircle in the Nyquist plot is depressed, which we attribute to surface roughness and the resulting distortion of the double layer [28].

3.2 Characterization of the corroded surface

Visual observation showed dark surfaces on all samples following the experiments compared with the shiny surfaces present before corrosion, although visible scale was not evident. Samples corroded in 5 and 20 wt% NaCl solutions were analyzed using BSE. Results for the 5 wt% NaCl corrosion sample reveal bare steel grains characterized by step-like dissolution surfaces (Fig. 3). Above and around these grains is a gauze-like material that appears to be a residual corrosion product (iron carbide; see below). We did not observe a distinct corrosion scale.

Surprisingly, a corrosion scale was observed at 20 wt% NaCl (Fig. 4). The BSE image shows the same gauze-like iron carbide corrosion residue (e.g., B of Fig. 4), but it also reveals smooth, rounded grains in contrast to the step-like surfaces of the bare steel grains (Fig. 3). These rounded grains (e.g., A of Fig. 4) appear to lie on top of the steel surface, forming a scale that is cracked in places, perhaps as a result of desiccation.

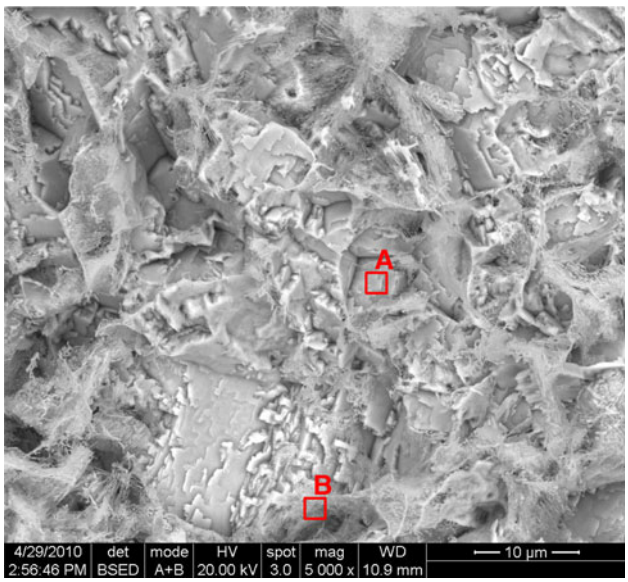

Fig. 3 BSE images of corroded steel surface exposed to 5 wt% NaCl solutions at pH = 4, $T = 25$ °C, $pCO_2 = 0.97$ bar, and $t = 4$ days. An example of a bare steel grain with stepped surface is visible in the *lower left* of the image (and within area *A*). Residual iron carbide is present as a gauze-like material, such as is visible on the *left side* of the image (and within area *B*). Chemical analysis for areas *A* and *B* are given in Figs. 5 and 6, respectively

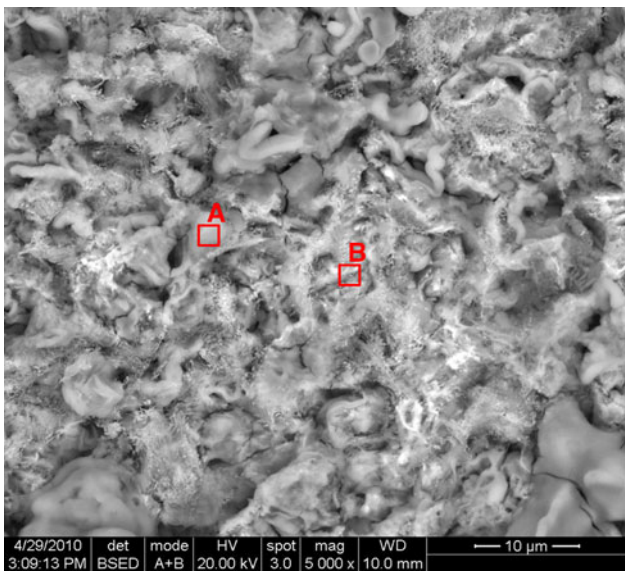

Fig. 4 BSE images of corroded steel surface exposed to 20 wt% NaCl solutions at pH = 4, $T = 25$ °C, $pCO_2 = 0.97$ bar, and $t = 3$ days. An example of smooth, rounded grain (scale) is visible in the *bottom-right* of the image (and within area *A*). Residual iron carbide is present as a gauze-like material, such as is visible in and adjacent to area *B*. Chemical analysis for areas *A* and *B* are given in Figs. 7 and 8, respectively

Chemical analysis by EDX of the surface of the sample corroded in 5 wt% NaCl showed that the surface was composed of bulk steel where carbon content was low

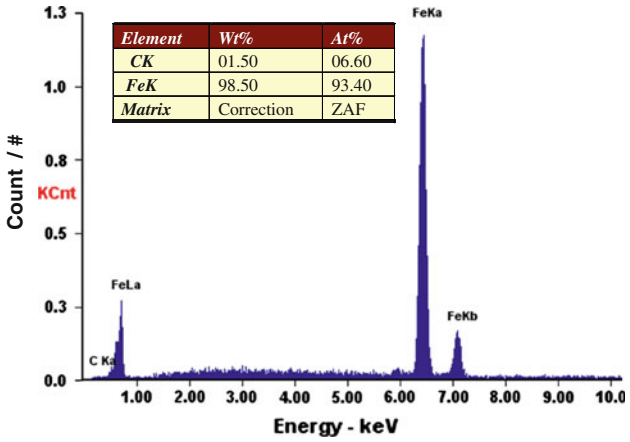

Fig. 5 EDX analysis of corroded steel surface exposed to 5 wt% NaCl solutions at area *A* in Fig. 3

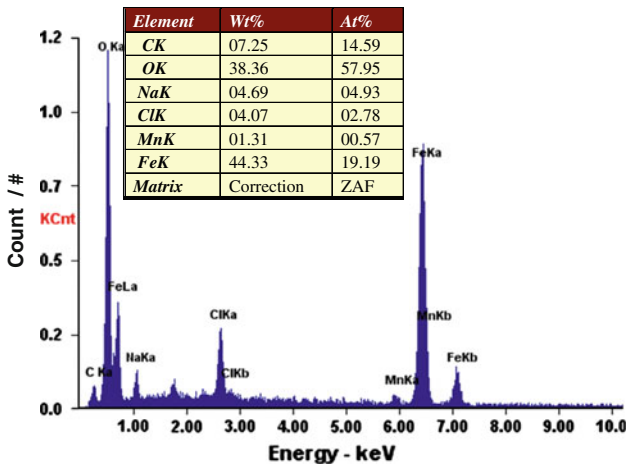

Fig. 7 EDX analysis of corroded steel surface exposed to 20 wt% NaCl solutions at area *A* in Fig. 4

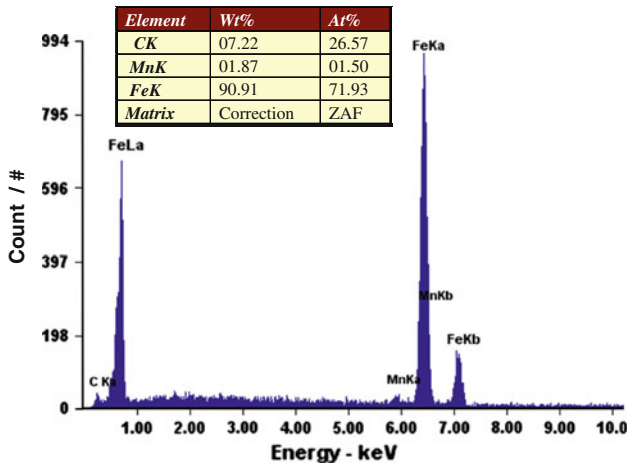

Fig. 6 EDX analysis of corroded steel surface exposed to 5 wt% NaCl solutions at area *B* in Fig. 4

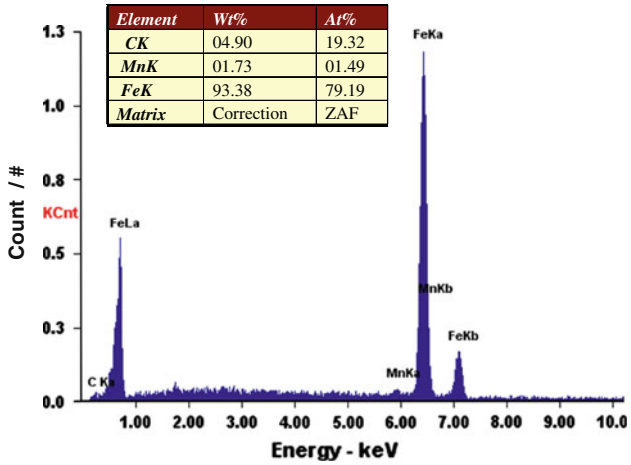

Fig. 8 EDX analysis of corroded steel surface exposed to 20 wt% NaCl solutions at area *B* in Fig. 4

(Fig. 5) and carbon-enriched material with carbon concentration four times higher than bulk steel (Fig. 6). The most likely carbon-enriched zone is a corrosion residue consisting of iron carbide, since no other element other than iron and carbon is observed. The manganese observed in Fig. 6 may be a corrosion residue (cf., Table 1), but may also have been derived from dissolution of the Hastelloy autoclave pressure vessel.

In contrast, EDX analysis of the sample surface exposed to 20 wt% NaCl shows that the crystalline corrosion product contains significant amounts of oxygen and carbon in addition to iron (Fig. 7; the sodium and chloride are contaminants from the aqueous solution). The remainder of the surface consists of carbon-enriched corrosion residue (Fig. 8). The EDX suggests that iron oxide and/or iron carbonate are present on the surface exposed to high-salinity brine. In a study of corrosion in deaerated aqueous solutions, Wang et al. [19] suggested that the corrosion scale was iron oxide. In order to determine the mineralogy of the corrosion scale, we conducted XRD as presented in the following section.

XRD were carried out to determine the mineralogy of the corrosion surfaces prepared at 0.5 and 20 wt% NaCl solutions. At 0.5 wt% NaCl concentration, only iron and the residual corrosion material iron carbide (Fe_3C) were observed (Fig. 9). A hump at 17–18° 2θ reflects an unidentified amorphous corrosion product. The absence of any crystalline corrosion scale is consistent with SEM observations showing only iron and residual carbide.

XRD analysis of the corrosion surface formed in 20 wt% NaCl solution revealed a weak broad peak near 35° 2θ consistent with magnetite (Fe_3O_4), in addition to

diffraction peaks for iron, residual iron carbide, and NaCl (Fig. 10). The possible magnetite is consistent with Wang et al. [19] observation of iron oxide in corrosion scale formed in deaerated brines. Our EDX analyses showing the presence of oxygen and carbon are consistent with XRD observation and indicate that the corrosion surface was composed of magnetite and iron carbide. We expect that the magnetite scale would act as a diffusion barrier, explaining why corrosion kinetics are independent of flow rate at 20 wt% NaCl.

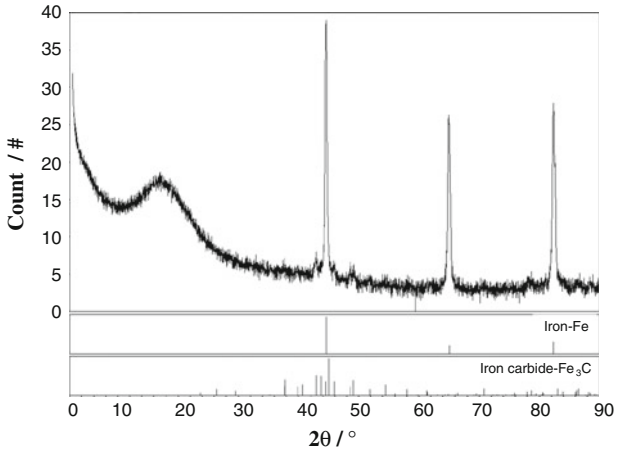

Fig. 9 XRD pattern and analysis of a corroded steel surface exposed to 0.5 wt% NaCl, pH = 4, $T = 25$ °C, $pCO_2 = 0.97$ bar, and $t = 5$ days

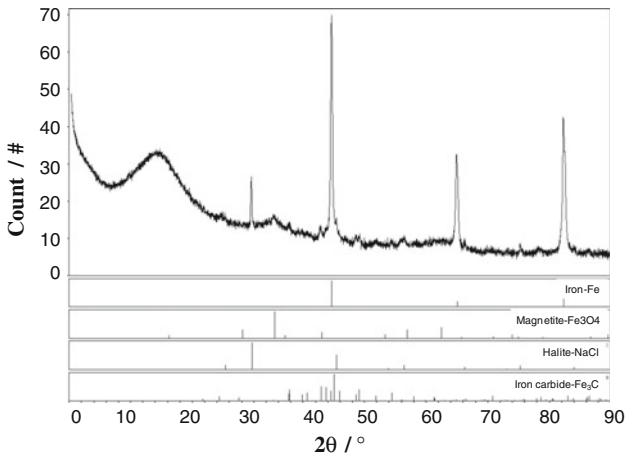

Fig. 10 XRD pattern and chemistry analysis of steel surface exposed to 20 wt% NaCl, pH = 4, $T = 25$ °C, $pCO_2 = 0.97$ bar, and $t = 3$ days

Interestingly, there was no XRD evidence of $FeCO_3$ scale, which is commonly seen in CO_2 environments. In order to investigate this phenomenon, we sampled the aqueous solutions after the corrosion experiments (Table 3) and used a water chemistry model [10] to calculate aqueous speciation and mineral stability at equilibrium with a 0.97 bar atmosphere of CO_2. The calculations showed that the iron carbonate concentration was at least 10,000 times lower than the saturation level for iron carbonate, consistent with the lack of iron carbonate scale.

4 Model simulation of salt effect on corrosion

As discussed in the introduction, chloride accelerates the anodic reaction of steel dissolution in aqueous systems lacking O_2 or CO_2, but reduces corrosion rates in O_2- or CO_2-bearing systems. In the case where oxygen is present, the corrosion rate decrease was attributed to the salting-out (reduction of gas solubility). Here we show using an electrochemical model that the reduction in CO_2-bearing environments can be explained by the "salting-out" effect.

We previously developed a coupled water chemistry–electrochemical corrosion model [10]. In the water chemistry model, Pitzer's activity model was used for the aqueous solution, and the model has the capability to accurately predict thermodynamics of the aqueous CO_2 system:

$$CO_{2(gas)} \rightleftarrows CO_{2(aq.)} \quad (5)$$

$$CO_{2(aq.)} + H_2O \rightleftarrows 2H_2CO_{3(aq.)} \quad (6)$$

$$H_2CO_{3(aq.)} \rightleftarrows HCO_3^-{}_{(aq.)} + H^+_{(aq.)} \quad (7)$$

$$HCO_3^-{}_{(aq.)} \rightleftarrows CO_3^{2-}{}_{(aq.)} + H^+_{(aq.)} \quad (8)$$

$$H_2O_{(aq.)} \rightleftarrows OH^-_{(aq.)} + H^+_{(aq.)} \quad (9)$$

The electrochemistry model simulates oxidation–reduction reactions involving the metal surface and

Table 3 Solution composition analysis using ion chromatography and ICP-OES

NaCl (wt%)	Cl^- (ppm)	Na^+ (ppm)	HCO_3^- (ppm)	CO_3^{2-} (ppm)	Fe^{2+} (ppm)	pH
0.5	3247	2036	0	<0.8	16	5.89
2	12080	7887	0	<0.8	11	4.84
5	28812	19862	20	<0.8	8	5.31
20	117841	88775	0	<0.8	1	5.27
20	121588	87312	24	<0.8	2	5.43

Bicarbonate and carbonate concentrations and pH were measured by titration in open air. pH values measured after equilibration with air

dissolved aqueous species. The significant cathodic reactions are carbonic acid, proton, and water reduction [10]:

$$2H_2CO_{3(aq.)} + 2e^- \rightarrow H_{2(g.)} + 2HCO_3^-{}_{(aq.)} \quad (10)$$

$$2H^+_{(aq.)} + 2e^- \rightarrow H_{2(gas)} \quad (11)$$

$$2H_2O_{(l.)} + 2e^- \rightarrow H_{2(gas)} + 2OH^-_{(aq.)} \quad (12)$$

The anodic activation reaction is the oxidative dissolution of iron:

$$Fe_{(s.)} \rightarrow Fe^{2+}_{(aq.)} + 2e^- \quad (13)$$

Sodium chloride plays a complicated role in corrosion kinetics. First, it can accelerate the corrosion process by forming intermediate corrosion species [18]. The second effect is that solution pH is decreased by adding more NaCl due to higher activity of H^+ [10–14], which accelerates corrosion kinetics. The third role is that it reduces CO_2 solubility, which leads to a slower corrosion. For example, a calculation for CO_2-bearing systems (Fig. 11) shows that concentration of dissolved CO_2 decreases as sodium chloride concentration increases under the conditions of our experiments. Our experimental results show that although pH is reduced by NaCl, the net effect is that corrosion rates are reduced by salt and indicate that the "salting-out" effect of NaCl dominates the other two competitive effects.

A comparison between our corrosion model and experimental data is shown in Fig. 12. The actual flow velocity was not modeled in the current experiments, as the current model only accounts for flow in cylindrical and pipe geometries. In these simulations, we approximated flow in our stirred reactor by using the rotational speed of cylindrical geometry samples. The model predicts that corrosion rate decreases as salt concentration increases until NaCl saturation is reached. Corrosion rates are predicted to be a function of flow rate at all concentrations. The model shows that corrosion rates are flow dependent at salt concentration lower than 20 wt%. Fair agreement with

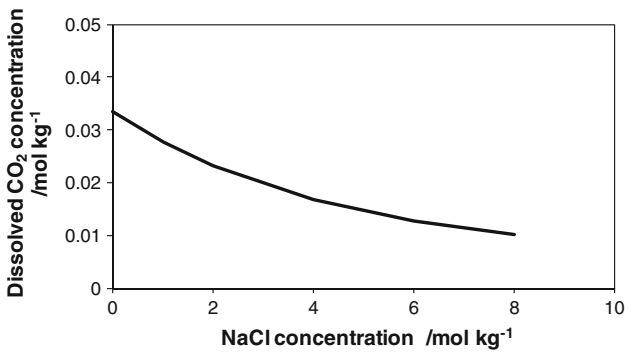

Fig. 11 Calculation of CO_2 solubility as a function of salt concentration at $T = 25$ °C, pH = 4, and $pCO_2 = 0.97$ bar

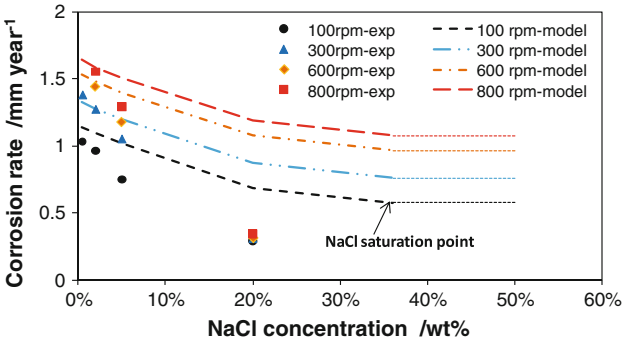

Fig. 12 Comparison of predicted and measured corrosion rate as a function of NaCl concentration at $T = 25$ °C, pH = 4, and $pCO_2 = 0.97$ bar

experimentally measured corrosion rate data was achieved. The model predicts the correct downward trend in corrosion rates, it correctly maintains the difference in corrosion rates as a function of fluid flow at 0–5 wt% NaCl, but does not predict as significant a decrease in corrosion as observed experimentally. This is a fair improvement over classical CO_2 corrosion models that have not considered NaCl effects [29, 30]. Those models do not include the non-ideality of the salt solution and thus predict a corrosion rate independent of NaCl concentration. The origin of the difference between the model and data is related to the incomplete model status of the water chemistry and electrochemistry. The model improves upon the classical model by incorporating non-ideal aqueous species activities instead of concentration. However, the current model does not include non-ideality in the electrochemical models except for pH. An additional area of improvement is needed in the representation of mass transfer, which is also based on concentration, not thermodynamic activity. We expect an improved fit to the data with a future version of the model that includes non-ideality in all aspects of the corrosion model.

At 20 wt% NaCl concentration, however, a more significant difference between model predictions and experimental data was observed: corrosion rates have almost no dependence on flow rates. The numerical model accounts only for bare surface corrosion and the simplest explanation for the observed flow-independent corrosion rates is formation of magnetite scale acting as a diffusion barrier.

The corrosion model also allows a comparison of potentiodynamic polarization curves as a function of NaCl concentration with literature observations. The model shows that cathodic reactions are retarded by sodium chloride (Fig. 13); and that anodic current densities are not significantly affected. Iron dissolution kinetics depend on solid steel, which is not concentration dependent. There are literature reports that anodic current densities also depend on pH as OH- is involved in the corrosion catalytic path

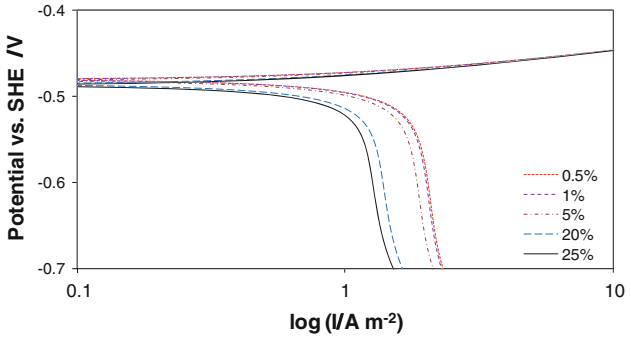

Fig. 13 Model prediction of polarization curves at $T = 25$ °C, pH = 4, and $pCO_2 = 0.97$ bar

[25]. However, in our experiments, a constant pH of 4 was maintained. On the other hand, the cathodic reactions reach a limiting mass transfer (the curves turn vertical in Fig. 13) at lower current densities with higher salt concentrations. Analysis of the model outputs indicates that this is due to decreased CO_2 or carbonic acid concentration in the solution as salt concentration increased (Fig. 11). The model calculation agrees with literature potentiodynamic measurement trends up to 20 wt% NaCl [23, 24]. At higher NaCl concentrations, our observations show that a magnetite-bearing scale forms that inhibits corrosion rates, and we expect that the measured anodic polarization curve should reach a maximum current density and then reverse toward lower densities at higher potentials.

5 Summary

Understanding and predicting corrosion rates in CO_2-bearing saline systems is important to industries such as wellbore operations in oil and gas production and in CO_2 sequestration. While significant study has been done previously on corrosion in deaerated and oxygenated brines, there are few studies of deaerated, CO_2-bearing brines. In this study, corrosion experiments were conducted as a function of NaCl concentration in CO_2-saturated brine in order to investigate the role of chloride in corrosion in CO_2 environments. A decreased corrosion rate was observed as salt concentration increased and flow rates of the aqueous solution decreased. However, corrosion rates were independent of flow rates in highly concentrated electrolyte ($\geq$20 wt% NaCl) solution. This was explained by the observation of an iron oxide corrosion scale found at 20 wt% NaCl concentration but not at lower salt concentrations. This scale was determined to be magnetite by X-ray diffraction. Our results indicate that the observation of flow-independence at 20 wt% NaCl is a result of a diffusion barrier formed by the magnetite scale.

We used a coupled water chemistry and corrosion model to show that CO_2 solubility was reduced significantly by increasing salt concentration, and that this accounted for the reduction of the corrosion rate with salt concentration in agreement with our observations and literature data [23, 24]. However, the model does not explain the flow-independence of corrosion rates at high salt concentration. This is because the magnetite scale (not considered in the model) created a diffusion barrier, resulting in corrosion rates that were independent of solution flow.

Acknowledgments The authors thank the Fossil Energy Program of the Department of Energy (FE-10-001) for funding support. The authors would like to acknowledge Michael S. Rearick from GGRL Lab (Geology Geochemistry Research Lab), Earth and Environmental Sciences Division, Los Alamos National Laboratory for his water chemistry analysis. The manuscript was significantly improved by comments from anonymous reviewers.

References

1. Pachauri RK, Reisinger A (2007) Climate change 2007: Synthesis report. Contribution of working groups I, II and III to the fourth assessment report of the intergovernmental panel on climate change. IPCC, Geneva
2. Bachu S (2000) Energy Convers Manag 41:953
3. Bachu S (2002) Energy Convers Manag 43:87
4. Carey JW, Wigand M, Chipera S et al (2007) Int J of Greenh Gas Con 1:75
5. Crow W, Carey JW, Gasda S et al (2010) Int J of Greenh Gas Con 4:186
6. Carey JW, Svec R, Grigg R et al (2010) Int J of Greenh Gas Con 4:272
7. Han J, Carey JW, Zhang J (2010) 9th Annual Conference for Carbon Capture and Sequestration, paper no# 361
8. Woollam RC, Hernandez SE (2006) SPE international oilfield corrosion symposium, paper no. 100673. Society of Petroleum Engineers, Aberdeen, UK
9. Nyborg R (2010) NACE CORROSION/2010, paper no. 10371.
10. Han J, Carey JW, Zhang J (2011) Int J of Greenh Gas Con. doi: 10.1016/j.ijggc.2011.02.005
11. Chin RJ, Nobe K (1972) J Electrochem Soc 119:1457
12. Darwish NA, Hilbert F, Lorenz WJ et al (1973) Electrochim Acta 18:421
13. Kuo HC, Nobe K (1978) J Electrochem Soc 125:853
14. MacFarlane DR, Smedley IS (1986) J Electrochem Soc 133:2240
15. Asakura S, Nobe K (1971) J Electrochem Soc 118:13
16. Burstein GT, Davies DH (1980) Corros Sci 20:1143
17. Burstein GT, Davies DH (1980) J Electrochem Soc 128:33
18. Ashley GW, Burstein GT (1991) Corrosion 47:908
19. Wang Z, Moore RC, Felmy AR et al (2001) Waste Manag 21:335
20. Cid M, Penuela A, Pett MC (1985) Mater Chem Phys 13:139
21. Foley RT (1970) Corrosion 26:58
22. Kirby GN (1995) Chem Eng Prog 91:47
23. Fang H, Nešić S, Brown BN (2007) NACE CORROSION/2007, paper no. 06372
24. Fang H, Brown BN, Nešić S (2010), NACE CORROSION/2010, paper no. 10276
25. Nešić S, Postlethwaite J, Olsen S (1996) Corrosion 54:280
26. Conway BE (1985). In: Conway BE, White RE, Bockris JO'M (eds) Modern aspects of electrochemistry, no. 16. Plenum Press, New York

27. Bockris JO'M, Drazic D, Despic AR (1961) Electrochim Acta 4:325
28. Harrington SP, Devine TM (2008) J Electrochem Soc 155:C381
29. De Waard C, Williams DE (1975) Corrosion 31:177
30. Norsok Standard M-506, CO_2 corrosion rate calculation model (Rev. 2). Available via DIALOG. http://www.standard.no/en/Sectors/Petroleum/NORSOK-Standard-Categories/M-Material/M-5061/. Accessed 15 Jan 2011